

Formation of coherent vortex streets and transport reduction in electron temperature gradient driven turbulence

M. Nakata,^{1,a)} T.-H. Watanabe,^{1,2} H. Sugama,^{1,2} and W. Horton³

¹*The Graduate University for Advanced Studies, Toki, Gifu 509-5292, Japan*

²*National Institute for Fusion Science, Toki, Gifu 509-5292, Japan*

³*Institute for Fusion Studies, The University of Texas at Austin, Austin, Texas 78712, USA*

(Received 13 October 2009; accepted 12 February 2010; published online 19 April 2010)

Vortex structures in slab electron temperature gradient (ETG) driven turbulence are investigated by means of a gyrokinetic simulation with high phase-space resolution. Depending on parameters that determine the eigenfrequency of the linear ETG modes, two different flow structures, i.e., statistically steady turbulence with a weak zonal flow and coherent vortex streets along a strong zonal flow, are observed. The former involves many isolated vortices and their mergers with complicated motion and leads to steady electron heat transport. When the latter is formed, phase difference and high wavenumber components of potential and temperature fluctuations are reduced, and the electron heat transport decreases significantly. It is also found that the phase matching with the potential fluctuation is correlated with the reduction in the imaginary part of the perturbed distribution function, and it occurs not only for the temperature fluctuation but also for any n th velocity moments. A traveling wave solution of a Hasegawa–Mima type equation derived from the gyrokinetic equation with the ETG agrees well with the coherent vortex streets found in the slab ETG turbulence. © 2010 American Institute of Physics. [doi:10.1063/1.3356048]

I. INTRODUCTION

Drift wave turbulence driven by microinstabilities such as ion temperature gradient (ITG) modes, electron temperature gradient (ETG) modes, and trapped electron modes have been extensively investigated by means of numerical simulations based on gyrokinetic or gyrofluid models to elucidate mechanisms of anomalous particle, heat, and momentum transport in the core region of magnetically confined plasmas.^{1,2} One of the remarkable results obtained by the ITG turbulence simulations is spontaneous generation of zonal flows, which regulate the turbulent transport through shearing of radially elongated vortices.³ The transport reduction by zonal flows leads to the nonlinear up-shift in the critical temperature gradient, which is larger than the linear stability threshold (that is, so-called Dimits shift). The existence of ion-scale zonal flows has been experimentally revealed by a direct measurement of electrostatic potential in helical plasmas.⁴

In the ETG turbulence, the gyro-Bohm scaling for $T_e = T_i$ predicts the smaller electron heat transport by a factor of $\sqrt{m_e/m_i}$ than the ion heat transport driven by the ITG turbulence. Many experimental observations, however, commonly indicate the strong anomaly of the electron heat transport, which could be of the same order as the ion one, even when the ion heat transport is reduced by the internal transport barrier.^{5,6} Although the linear ETG modes with an adiabatic ion response are isomorphic to the linear ITG modes with an adiabatic electron response, the nonlinear evolution of the ETG instability is quite different from that of the ITG one. This is because the intensity of nonlinearly generated zonal flows in the ETG turbulence is much lower than that in

the ITG turbulence due to the different responses to the zonal-flow potential.^{7,8} In contrast to the ITG turbulence with strong zonal flows, thus ETG turbulence involves various vortex structures, e.g., turbulent vortices, zonal flows, and radially elongated streamers, whose intensities depend on the magnetic shear and other parameters.⁹ Recently, a number of gyrokinetic simulations of the toroidal ETG turbulence have been performed and benchmarked with various simulation codes.^{10–13} Nevertheless, the saturation mechanism of the toroidal ETG instability under the strong magnetic shear and the estimation of resultant transport level are still open problems. We believe that detailed analyses of the vortex structures and the velocity-space structures of the distribution function are necessary for a better understanding of the ETG driven turbulent transport.

Zonal-flow dynamics and the properties of large-scale coherent vortex structures in the slab ETG turbulence have also been discussed by means of gyrokinetic and gyrofluid simulations.^{14–19} It has been pointed out that the weak magnetic shear is important for the zonal-flow generation, while the positive magnetic shear leads to the streamer formation.^{14,15} The scale length of zonal flow is characterized by the Rhines scaling, which is proportional to the density gradient scale length L_n , where the electron heat transport decreases with increasing of L_n .¹⁶ The statistical analyses for the ETG turbulence dominated by zonal flows reveal the phase matching between potential and pressure fluctuations, which is related to the reduction in the radial heat flux and the fractal dimension of the turbulent fluctuations.^{17,18} It has also been pointed out that in addition to the zonal flows, the dynamics of nonlinearly excited long wavelength modes is important for the saturation of the ETG instability and for the regulation of the electron heat transport.¹⁹

^{a)}Electronic mail: nakata.motoki@nifs.ac.jp.

In the present study, by means of the gyrokinetic Vlasov simulations, we investigate vortex structures of the slab ETG turbulence and velocity-space structures of the distribution function in detail. The nonlinear gyrokinetic simulations with high phase-space resolution shown below enable us to examine the entropy balance relation in the slab ETG turbulence with zonal-flow generation, while it has been investigated for the collisionless and weakly collisional slab ITG turbulence.^{20–23} Then, we discuss the role of zonal flows in the statistically steady turbulence and the transition of vortex structure from turbulent vortices to coherent vortex streets accompanied with the significant reduction of the electron heat transport. The transport reduction in the coherent state is also studied from the viewpoint of structural change of the perturbed distribution function in the velocity-space. In the latter part of this paper, the coherent vortex streets found in the nonlinear simulation are compared with a traveling wave solution of a Hasegawa–Mima (HM) type equation.

The remainder of this paper is organized as follows. Gyrokinetic models used in the present study are described in Sec. II. Simulation results are presented in Sec. III, where the statistically steady state with weak zonal flows in the slab ETG turbulence is compared with that in the slab ITG turbulence in Sec. III A. The spontaneous formation of the coherent vortex streets and resultant transport reduction, which are found in parameters different from those in Sec. III A, are discussed in Sec. III B. The derivation of a fluid model describing the coherent vortex streets and the application to the nonlinear simulation results are given in Secs. IV A and IV B, respectively. Finally, the results obtained are summarized in Sec. V.

II. GYROKINETIC MODEL

The electrostatic gyrokinetic equation^{24,25} for electron gyrocenter distribution function $\mathcal{F}_e^{(g)} = \mathcal{F}_e^{(g)}(\mathbf{x}, v_\perp, v_\parallel, t)$ in an uniform magnetic field $\mathbf{B} = B\mathbf{b}$ is written as

$$\begin{aligned} \frac{\partial \mathcal{F}_e^{(g)}}{\partial t} + v_\parallel \mathbf{b} \cdot \nabla \mathcal{F}_e^{(g)} + \frac{c}{B} \mathbf{b} \times \nabla \langle \phi(\mathbf{x} + \boldsymbol{\rho}_e) \rangle_g \cdot \nabla \mathcal{F}_e^{(g)} \\ + \frac{e}{m_e} \mathbf{b} \cdot \nabla \langle \phi(\mathbf{x} + \boldsymbol{\rho}_e) \rangle_g \frac{\partial \mathcal{F}_e^{(g)}}{\partial v_\parallel} = 0, \end{aligned} \quad (1)$$

where \mathbf{x} , $\boldsymbol{\rho}_e$, c , e , and m_e are the gyrocenter position, the electron gyroradius vector, the speed of light, the elementary charge, and the electron mass, respectively. The gyroaveraged electrostatic potential is denoted by $\langle \phi(\mathbf{x} + \boldsymbol{\rho}_e) \rangle_g$, where $\langle \cdots \rangle_g$ means the gyrophase average for a fixed gyrocenter position. The total gyrocenter distribution function $\mathcal{F}_e^{(g)}$ is divided into equilibrium and perturbation parts: $\mathcal{F}_e^{(g)} = F + \delta f^{(g)}$. We assume that the former is given by the Maxwellian distribution,

$$F = F_M(\mathbf{x}, v_\perp, v_\parallel) = n_0 \left(\frac{m_e}{2\pi T_e} \right)^{3/2} \exp\left(-\frac{m_e(v_\perp^2 + v_\parallel^2)}{2T_e} \right), \quad (2)$$

where n_0 and T_e denote the equilibrium density and the electron temperature. The perturbed distribution function and the

potential fluctuation are written in terms of the Fourier expansions,

$$\delta f^{(g)}(\mathbf{x}, v_\perp, v_\parallel, t) = \sum_k \delta f_k^{(g)}(v_\perp, v_\parallel, t) e^{i\mathbf{k} \cdot \mathbf{x}}, \quad (3)$$

$$\phi(\mathbf{x} + \boldsymbol{\rho}_e, t) = \sum_k \delta \phi_k(t) e^{i\mathbf{k} \cdot (\mathbf{x} + \boldsymbol{\rho}_e)}, \quad (4)$$

where the equilibrium part of the potential is not considered here. In order to keep high resolution in the real space and the v_\parallel -space, we assume that v_\perp -dependence of $\delta f_k^{(g)}$ is given by the Maxwellian distribution, i.e., $\delta f_k^{(g)}(v_\perp, v_\parallel, t) = F_{M\perp}(v_\perp) \delta f_k(v_\parallel, t)$, where $F_{M\perp} \equiv (m_e/2\pi T_e) \times \exp(-m_e v_\perp^2/2T_e)$. The gradient scale lengths of the equilibrium density $L_n \equiv -(d \ln n_0/dx)^{-1}$ and the equilibrium temperature $L_T \equiv -(d \ln T_e/dx)^{-1}$, which are much longer than fluctuation wavelengths in the direction perpendicular to the magnetic field $\lambda = 2\pi/|\mathbf{k}_\perp|$, are set to be constant.

We consider a periodic two-dimensional slab configuration where the plasma is assumed to be homogeneous in the z -direction. The magnetic field \mathbf{B} is set in the y - z plane such that $\mathbf{B} = B(\mathbf{e}_z \cos \theta + \mathbf{e}_y \sin \theta) \approx B(\mathbf{e}_z + \theta \mathbf{e}_y)$ for $\theta \ll 1$, where \mathbf{e}_y , \mathbf{e}_z , and θ denote the basis vectors in the y - and z -directions and the tilt angle of the field line, respectively. Substituting Eqs. (2)–(4) into Eq. (1) and integrating over the v_\perp -space, one can obtain the gyrokinetic equation for the perturbed distribution function $\delta f_k(v_\parallel, t)$ written in the wave-number space as

$$\begin{aligned} \left(\frac{\partial}{\partial t} + i k_\parallel v_\parallel \right) \delta f_k - \frac{c}{B} \sum_{\mathbf{k}' + \mathbf{k}'' = \mathbf{k}} \mathbf{b} \cdot (\mathbf{k}' \times \mathbf{k}'') \delta \psi_{\mathbf{k}'} \delta f_{\mathbf{k}''} - C_\parallel(\delta f_k) \\ = -i \left\{ \omega_{*e} \left[1 + \eta_e \left(\frac{m_e v_\parallel^2}{2T_e} - \frac{1}{2} - \frac{b_k}{2} \right) \right] - k_\parallel v_\parallel \right\} F_{M\parallel} \frac{e \delta \psi_k}{T_e}. \end{aligned} \quad (5)$$

Here, $k_\parallel \equiv \mathbf{k} \cdot \mathbf{b} \approx \theta k_y$ is the parallel wavenumber (k_z vanishes because of the translational symmetry in the z -direction), $b_k \equiv k_\perp^2 \rho_{te}^2$ is the square of the perpendicular wavenumber normalized by the electron thermal gyroradius $\rho_{te} \equiv v_{te}/\Omega_e$, where $v_{te} \equiv (T_e/m_e)^{1/2}$ and $\Omega_e \equiv eB/m_e c$ are the electron thermal speed and the electron gyrofrequency, respectively. Inhomogeneities of n_0 and T_e in the x -direction are taken into account through the electron drift frequency $\omega_{*e} \equiv -(cT_e/eB)\mathbf{k} \cdot \mathbf{b} \times \nabla \ln n_0$ and the parameter $\eta_e \equiv L_n/L_T$. The gyroaveraged potential integrated over the v_\perp -space is denoted by $\delta \psi_k \equiv \delta \phi_k \exp(-b_k/2)$, where the factor $\exp(-b_k/2)$ arises from the finite-Larmor-radius (FLR) effect. The Maxwellian distribution of v_\parallel is denoted by $F_{M\parallel} \equiv n_0 (m_e/2\pi T_e)^{1/2} \exp(-m_e v_\parallel^2/2T_e)$. In the derivation of the above equation, the parallel nonlinearity $(e/m_e)\mathbf{b} \cdot \nabla \langle \phi(\mathbf{x} + \boldsymbol{\rho}_e) \rangle_g \partial \delta f^{(g)}/\partial v_\parallel$ included in Eq. (1) is neglected because of the gyrokinetic ordering $k_\parallel/k_\perp \sim \rho_{te}/L_T \ll 1$. In order to maintain this ordering, the value of the tilt angle θ is expressed by the dimensionless parameter $\Theta \equiv k_\parallel L_T/k_y \rho_{te} \approx \theta L_T/\rho_{te}$.

In the present model, a weak but finite collisionality effect is introduced in terms of a model collision operator $C_\parallel(\delta f_k)$ as follows:

$$C_{\parallel}(\delta f_k) = \nu_e \frac{\partial}{\partial v_{\parallel}} \left(v_{te}^2 \frac{\partial}{\partial v_{\parallel}} + v_{\parallel} \right) \delta f_k. \quad (6)$$

Here, ν_e denotes the electron collision frequency. The collision operator acting on δf_k smooths out the fine-scale fluctuations in the v_{\parallel} -space. Although the above collision operator does not conserve the momentum and the energy, its influence on the main results shown below, such as the transport level, are not crucial as long as $\nu_e L_T / v_{te} \ll 1$.²¹

The electrostatic potential is determined by the quasineutrality condition $\delta n_e = \delta n_i$, where the Laplacian term $\nabla^2 \delta \phi$ in the Poisson equation is neglected. Since the potential should be evaluated at the particle position, not at the gyrocenter position, the distribution function should be transformed from the gyrocenter coordinates to the particle ones. The relation between the particle distribution function $\delta f_k^{(p)}$ and the gyrocenter distribution function $\delta f_k^{(g)}$ is given by

$$\delta f_{sk}^{(p)} = \delta f_{sk}^{(g)} e^{-ik \cdot \rho_s} - \frac{e_s \delta \phi_k}{T_s} [1 - J_0(k_{\perp} \rho_s) e^{-ik \cdot \rho_s}] F_{Ms}, \quad (7)$$

where the subscript s represents particle species [$s = \{i, e\}$ for ions and electrons] so that e_s has a sign of the electric charge for each species and $J_0(z)$ is the zeroth-order Bessel function. The last group of terms on the right-hand side represents the polarization due to the potential fluctuations. By taking the velocity-space integral of Eq. (7) for electrons, one can obtain the electron density fluctuation in the particle coordinates

$$\begin{aligned} \delta n_{ek} &= \int d\mathbf{v} \left\{ \delta f_{ek}^{(g)} e^{-ik \cdot \rho_e} + \frac{e \delta \phi_k}{T_e} [1 - J_0(k_{\perp} \rho_e) e^{-ik \cdot \rho_e}] F_{Me} \right\} \\ &= e^{-b_{ek}/2} \int dv_{\parallel} \delta f_{ek} + n_0 \frac{e \delta \phi_k}{T_e} [1 - \Gamma_0(b_{ek})], \end{aligned} \quad (8)$$

where Γ_0 is defined by $\Gamma_0(z) \equiv I_0(z) \exp(-z)$ with the zeroth-order modified Bessel function $I_0(z)$. Similarly, the ion particle density fluctuation is given as

$$\begin{aligned} \delta n_{ik} &= e^{-b_{ik}/2} \int dv_{\parallel} \delta f_{ik} - n_0 \frac{e \delta \phi_k}{T_i} [1 - \Gamma_0(b_{ik})] \\ &\simeq -n_0 \frac{e \delta \phi_k}{T_i} \quad (k_{\perp} \rho_{ti} \gg 1). \end{aligned} \quad (9)$$

Since the characteristic wavelength in the ETG turbulence, which is comparable to the electron gyroradius, is much shorter than the ion gyroradius, i.e., $k_{\perp} \rho_{ti} \gg 1$, the ion response to the potential fluctuation reduces to the adiabatic one as shown in the last equality of Eq. (9). Combining Eqs. (8) and (9), the quasineutrality condition $\delta n_e = \delta n_i$ with the adiabatic ion response is rewritten as

$$\int dv_{\parallel} \delta f_{ek} = -e^{b_{ek}/2} \left\{ 1 + \frac{T_e}{T_i} - \Gamma(b_{ek}) \right\} n_0 \frac{e \delta \phi_k}{T_e}. \quad (10)$$

In ITG turbulence simulations, the electron response is often assumed to be adiabatic except for the zonal-flow component of $k_{\parallel} = k_y = 0$. The electron response in ITG turbulence is denoted by $\delta n_e = n_0 e (\delta \phi - \langle \langle \delta \phi \rangle \rangle) / T_e$, while the ion response in the ETG turbulence is given by Eq. (9), where $\langle \langle \dots \rangle \rangle$ means

a flux surface average. The physical pictures of the responses to the zonal-flow potential in ITG and ETG turbulence are quite different. In the ITG turbulence, electrons do not respond to the zonal-flow potential, i.e., $\delta n_{ek_{\parallel}=0} = 0$, because the parallel electric field E_{\parallel} vanishes for the mode of $k_{\parallel} = 0$. On the other hand, ions in the ETG turbulence can move in the perpendicular direction because of the large ion gyroradius, i.e., $k_{\perp} \rho_{ti} \gg 1$ even if $E_{\parallel} = 0$. As a result of the different responses of ions and electrons to the zonal-flow potential, the relative intensity of the zonal flow in the ETG turbulence is lower than that in the ITG turbulence.³

From the closed set of equations described in Eqs. (5) and (10), one can derive a balance equation with respect to the entropy variable $\delta S \equiv S_M - \langle S_m \rangle$, where $\langle \dots \rangle$ means the ensemble average.^{26,27} The macroscopic and the microscopic entropy per unit volume are defined by $S_M \equiv -\int d\mathbf{v} F_M \ln F_M$ and $S_m \equiv -\int d\mathbf{v} \mathcal{F}_e^{(g)} \ln \mathcal{F}_e^{(g)}$, respectively. Then, one finds

$$\delta S = S_M - \langle S_m \rangle \simeq \int d\mathbf{v} \left\langle \frac{\delta \mathcal{F}_e^{(g)}}{2F_M} \right\rangle = \sum_k \int dv_{\parallel} \frac{|\delta f_k|^2}{2F_{M\parallel}}, \quad (11)$$

which is correct to $\mathcal{O}(\delta \mathcal{F}_e^{(g)2})$. Here, we assume the turbulent fluctuations to be statistically homogeneous in space. Thus, the ensemble average is replaced by the spatial average in the last equality of Eq. (11). Taking the v_{\parallel} -space integral and the summation over \mathbf{k} in Eq. (5) multiplied by $\delta f_k^* / F_{M\parallel}$ (where the asterisk denotes the complex conjugate), one can obtain the entropy balance equation,

$$\frac{d}{dt} (\delta S + W) = Q_e + D, \quad (12)$$

by use of Eq. (10). The quantities W , Q_e , and D denote the potential energy, the electron heat flux, and the collisional dissipation, respectively. The definitions are as follows:

$$W = \sum_k W_k = \sum_k \frac{n_0}{2} \left(1 + \frac{T_e}{T_i} - \Gamma_0(b_k) \right) \left| \frac{e \delta \phi_k}{T_e} \right|^2, \quad (13)$$

$$\begin{aligned} Q_e &= \frac{\mathbf{q}_{\perp e}}{T_e} \cdot (-\nabla \ln T_e) \\ &= \sum_k \frac{c}{B} \frac{d \ln T_e}{dx} \text{Re} \left[ik_y \delta \psi_k \int dv_{\parallel} \left(\frac{m_e v_{\parallel}^2}{2T_e} - \frac{1}{2} \right) \delta f_k^* \right] \\ &= n_0 \left(\frac{d \ln T_e}{dx} \right)^2 \sum_k \chi_{ek}, \end{aligned} \quad (14)$$

$$D = \sum_k \int dv_{\parallel} C_{\parallel}(\delta f_k) \frac{\delta f_k^*}{F_{M\parallel}}, \quad (15)$$

where $\mathbf{q}_{\perp e}$ denotes the electron perpendicular heat flux due to the $\mathbf{E} \times \mathbf{B}$ convection. The electron heat transport coefficient is defined by $\chi_e = \sum_k \chi_{ek} = \mathbf{q}_{\perp e} \cdot \mathbf{e}_x / (n_0 T_e / L_T)$, where \mathbf{e}_x denotes the basis vector in the x -direction. The production, transfer, and dissipation processes of δS have been thoroughly investigated for the slab ITG turbulence.²¹ The entropy variable δS is generated by the turbulent heat transport Q_e in macrovelocity scale; then it cascades to microvelocity scale through

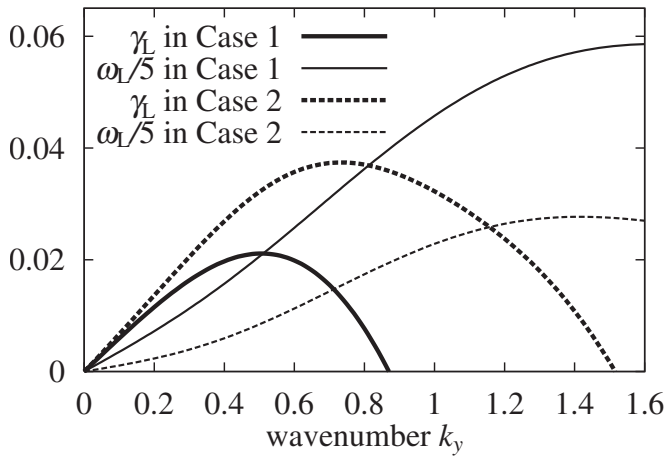


FIG. 1. Growth rates γ_L and real frequencies ω_L of the linear ETG modes for $k_x=0$ in case 1 ($\eta_e=6$, $\Theta=1/6$) and case 2 ($\eta_e=10$, $\Theta=1/20$).

the phase mixing process caused by the parallel advection term $ik_{\parallel}v_{\parallel}\delta f_k$ in Eq. (5). Finally, the entropy variable is dissipated by the collision in the microvelocity scale. The entropy balance relation also provides us a good measure for the accuracy of the nonlinear simulation.

In the followings, physical quantities are normalized as $x=x'/\rho_{te}$, $y=y'/\rho_{te}$, $v_{\parallel}=v'_{\parallel}/v_{te}$, $t=t'v_{te}/L_T$, $v_e=v'_eL_T/v_{te}$, $F_{M\parallel}=F'_{M\parallel}v_{te}/n_0$, $\delta f_k=\delta f'_kL_Tv_{te}/\rho_{te}n_0$, and $\delta\phi_k=e\delta\phi'_k\times L_T/T_e\rho_{te}$, where the prime means a dimensional quantity. In the numerical simulations, time integrations are carried out by the fourth-order Runge–Kutta–Gill method with appropriate time step. The nonlinear advection term is calculated by means of the spectral method with 3/2-rule for the dealiasing in the wavenumber space. In order to keep high phase-space resolution, our code is parallelized with respect to the v_{\parallel} -coordinates, and the fourth-order central finite difference methods are used for evaluating the velocity-space derivatives in the collision operator. The nonlinear simulations have been carried out for two cases which have different dimensionless parameters η_e and Θ . The detailed simulation conditions for each parameter are given in the Sec. III A.

III. NONLINEAR SIMULATIONS

A. Physical and numerical parameters

Physical and numerical parameters for nonlinear simulations of the slab ETG turbulence are summarized below. We consider two sets of the physical parameters $\{\eta_e=6$, $\Theta=1/6\}$ (case 1) and $\{\eta_e=10$, $\Theta=1/20\}$ (case 2). The linear growth rate γ_L and real frequency ω_L for the two cases are plotted for k_y in Fig. 1. Here, we set $k_x=0$ because the finite k_x has a stabilizing effect. It is found that case 2 has rela-

TABLE I. Parameters used for nonlinear simulations.

	η_e	Θ	v_{\parallel} -grids	$\gamma_{L,\max}$	v_e
Case 1	6	1/6	1025	0.021	2.08×10^{-4}
Case 2	10	1/20	2049	0.037	1.25×10^{-4}

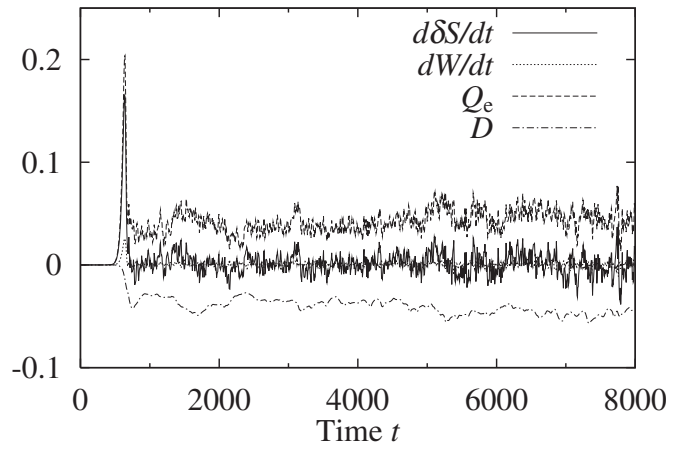


FIG. 2. Time evolution of each term in Eq. (12), $d(\delta S)/dt$, dW/dt , Q_e , and D in case 1.

tively lower real frequencies, larger growth rates, and a wider range of the unstable modes than case 1. The parameters used for nonlinear simulations are summarized in Table I. Here, sufficiently small collision frequency ν_e , which does not affect the linear growth rates and the real frequencies, is introduced in both cases. Also, we set $\tau\equiv T_e/T_i=1$. The number of modes in the wavenumber space and the minimum and maximum wavenumbers are set to be $(N_{k_x}, N_{k_y})=(129, 257)$, $k_{\min}=0.05$, and $k_{\max}=6.4$, respectively. The range of v_{\parallel} -coordinates is $|v_{\parallel}|\leq v_{\max}=10$. Furthermore, the simulation domain is set to be a square with $L_x=L_y=40\pi\rho_{te}$. In the ITG turbulence, as will be discussed in Sec. III B, the parameters are the same as those in the slab ETG turbulence of case 1, except for the use of the ion thermal gyroradius ρ_{ti} on the normalizations.

B. Steady turbulence and zonal flows

Simulation results for case 1 as well as the comparison between slab ETG and ITG turbulence are shown and discussed below. Time evolution of each term in Eq. (12), i.e., $d(\delta S)/dt$, dW/dt , Q_e , and D is plotted in Fig. 2. It is confirmed that the entropy balance relation described in Eq. (12) is accurately satisfied within an error less than 1% with respect to the amplitude of the collisional dissipation. In the nonlinear phase ($t\geq 700$), one can find a statistically steady state in the entropy balance, where the mean heat transport balances with the mean collisional dissipation, namely, $\overline{Q_e}\approx -\overline{D}$, while $\overline{d(\delta S)/dt}\approx \overline{dW/dt}\approx 0$ (the overline denotes the time average for $t\geq 1000$). The statistically steady state of slab ITG turbulence was confirmed by Watanabe and Sugama,²¹ where the zonal-flow components of the distribution function were not included for studying the entropy balance with strong ion heat transport. The present simulation demonstrates that the similar steady state with finite electron heat transport exists in the slab ETG turbulence including zonal flows self-consistently.

The time evolutions of the heat transport coefficients χ_s are shown in Fig. 3, where s denotes the particle species. Here, $\chi_{e,nz}$ and χ_e represent the results without and with the zonal-flow generation, respectively. In the former case, the

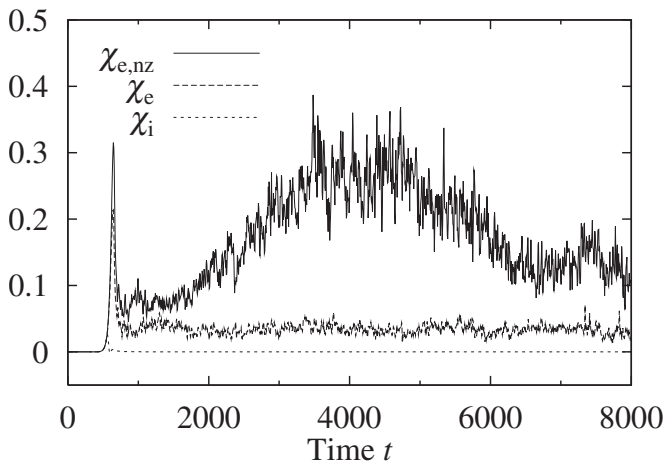


FIG. 3. Time evolutions of the transport coefficients $\chi_{e,nz}$ (ETG without zonal flows), χ_e (ETG with zonal flows), and χ_i (ITG with zonal flows), where the gyro-Bohm units $\rho_{is}^2 v_{is}/L_T$ ($s=e,i$) are used.

zonal-flow components of the perturbed distribution function $\delta f_{k_x, k_y=0}$ are artificially neglected. In addition, a slab ITG case with the zonal-flow generation is also plotted as χ_i in the figure. The saturation levels of the transport coefficients are $\overline{\chi_{e,nz}} = 1.34 \times 10^{-1} [\rho_{ie}^2 v_{ie}/L_T]$, $\overline{\chi_e} = 4.65 \times 10^{-2} [\rho_{ie}^2 v_{ie}/L_T]$, and $\overline{\chi_i} = 4.36 \times 10^{-5} [\rho_{ii}^2 v_{ii}/L_T]$, respectively, where they are evaluated by taking the time average for $6000 \leq t \leq 8000$. We find a quite small ratio of saturation levels $\overline{\chi_i}/\overline{\chi_e} \approx 9.38 \sqrt{m_i/m_e} \times 10^{-4} \approx 0.04$. This is because the zonal flow driven by the slab ITG turbulence is much stronger than that driven by the slab ETG turbulence due to the difference in the response to the zonal-flow potential $\delta \phi_{k_x, k_y=0}$ as described in Sec. II. Also, in the present slab configuration with the constant magnetic field, the zonal-flow damping due to the neoclassical polarization is not included. Therefore, the strong zonal flow is driven by the slab ITG turbulence and sustained for a long time. The time evolution of $\chi_{e,nz}$ indicates the higher level and the slow time-variation, while the value of χ_e reaches to the steady state. The averaged value $\overline{\chi_{e,nz}}$ is about 2.9 times larger than $\overline{\chi_e}$. These results suggest that the weak but finite zonal flows driven by the slab ETG turbulence play a major role in regulating the slow time-variation and in realizing the steady transport.

Comparisons of the cases with and without zonal flows provide us a clear understanding of the role of the zonal flow in regulating the turbulent transport. Figures 4(a)–4(c) show the wavenumber spectra of the potential energy $W_{k_x, k_y=0}$, $W_{k_x=0, k_y}$ [see Eq. (13)] and the transport coefficient $|\chi_{ek_x=0, k_y}|$ [see Eq. (14)], respectively, where the amplitudes are averaged over $3000 \leq t \leq 5000$. In Fig. 4(b), one can see a much larger amplitude of the $(k_x=0, k_y=k_{\min}=0.05)$ -mode compared to the other modes in the case without zonal flows, while its amplitude significantly decreases by a factor of about 30 in the case with zonal flows. A similar reduction is also found for $|\chi_{ek_x=0, k_y=k_{\min}}|$ in Fig. 4(c). The correlation between W_k and $|\chi_{ek}|$ indicates that the high level of $\chi_{e,nz}$ with the slow time-variation shown in Fig. 3 is mainly caused by low- k modes, where the $(k_x=0, k_y=k_{\min})$ -mode makes the largest contribution to the heat transport. The zonal flows

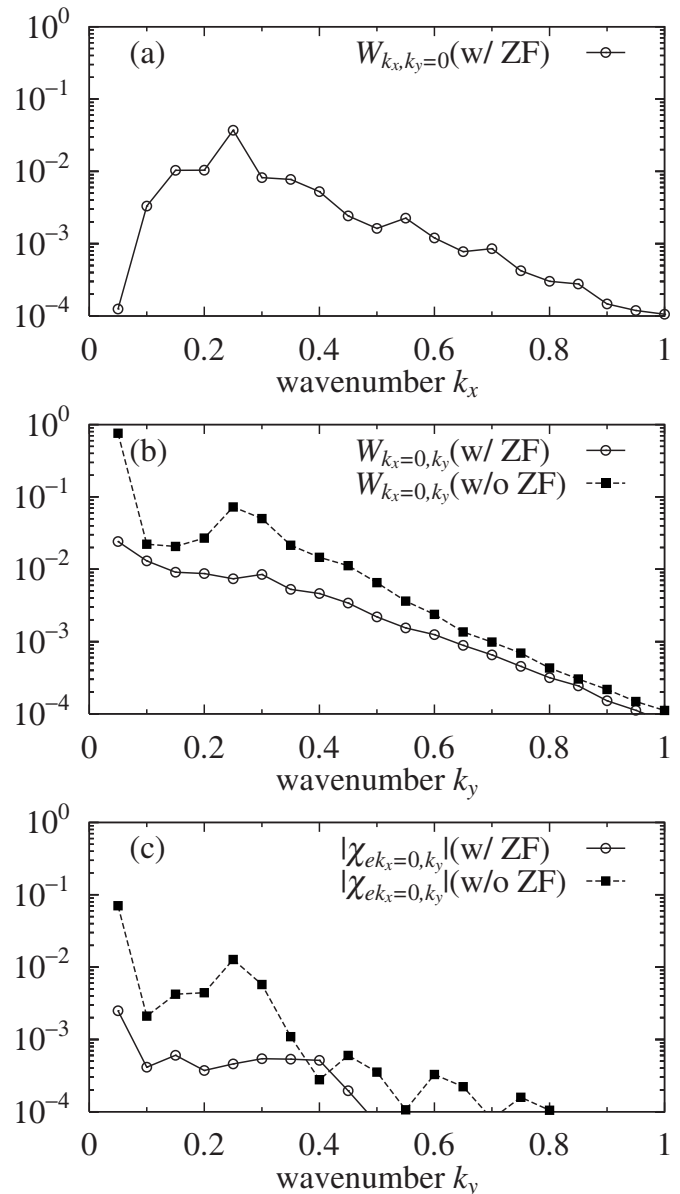


FIG. 4. The wavenumber spectra of the potential energy (a) $W_{k_x, k_y=0}$, (b) $W_{k_x=0, k_y}$, and the transport coefficient (c) $|\chi_{ek_x=0, k_y}|$ in the cases with and without zonal flows, where the amplitudes are averaged over $3000 \leq t \leq 5000$. The units $(\rho_{ie}/L_T)^2 (T_e/e)^2$ and $\rho_{ie}^2 v_{ie}/L_T$ are used for W_k and χ_{ek} , respectively.

with finite amplitudes shown in Fig. 4(a) suppress the low- k modes and reduce the transport level. Also, the contribution of $|\chi_{ek_x=0, k_y=k_{\min}}|$ to the total χ_e , that is, 27% in the case without zonal flows, decreases to 7% in the case with zonal flows. The reduction in the amplitudes of low- k modes by zonal flows lead to the steady χ_e .

The different evolutions of turbulent transport and the role of the zonal flow discussed above are also understood from the comparison of vortex structures. Color contours of the electrostatic potential fluctuations on the (x, y) -plane at $t=4980$ are shown in Figs. 5(a)–5(c) for the above three cases [(a) ETG without zonal flows, (b) ETG with zonal flows, and (c) ITG with zonal flows], respectively. In Fig. 5(a), one can see the formation of isolated vortices with the positive and the negative signs of the potential values. The

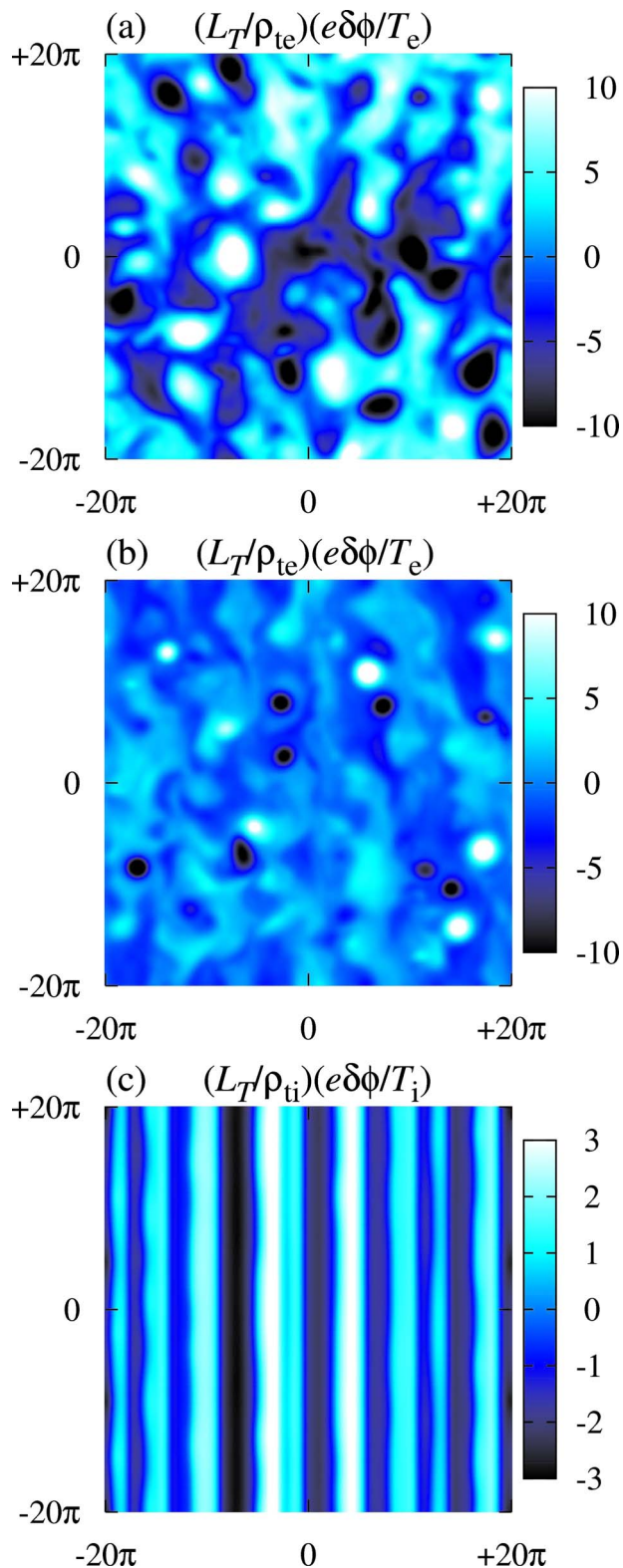


FIG. 5. (Color online) Contours of the normalized potential fluctuations at $t=4980$ in (a) ETG without zonal flows, (b) ETG with zonal flows, and (c) ITG with zonal flows.

size and amplitude of each vortex are typically $\Delta_{\text{vortex}} \approx 8[\rho_{te}]$ and $|\delta\phi|_{\text{vortex}} \approx 18[\rho_{te}T_e/L_T e]$, respectively. In addition, the $(k_x=0, k_y=k_{\text{min}})$ -mode, which makes a dominant contribution to the heat transport, is clearly observed behind the isolated vortices. The isolated vortices are also observed

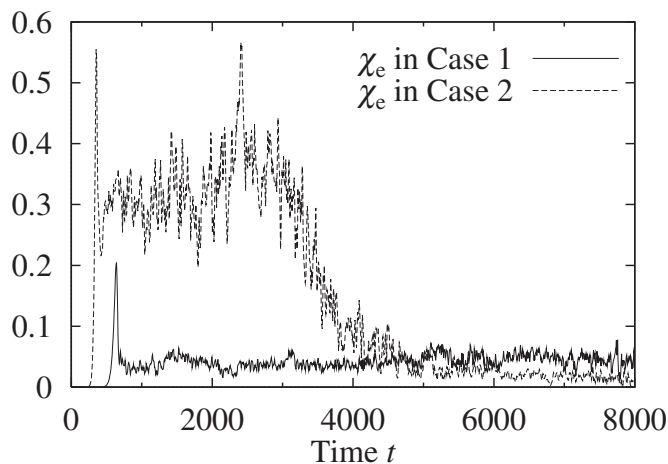


FIG. 6. Comparison of the time evolutions of the transport coefficients χ_e in case 1 and case 2, where the gyro-Bohm units $\rho_{te}^2 v_{te}/L_T$ are used.

in Fig. 5(b), where the typical size and amplitude of each vortex are slightly smaller than those found in the case without zonal flows. However, the $(k_x=0, k_y=k_{\text{min}})$ -mode no longer appears in the present case because it is suppressed by the zonal flows with finite amplitudes. Also, the isolated vortices exhibit the complicated motion and their mergers. Mergers of like-signed vortices have also been observed in the two-dimensional decaying plasma turbulence with HM model (see, for example, Refs. 16 and 28). In the present case, the zeroth velocity moment of the gyrokinetic equation used here includes the similar nonlinearity to that in the HM equation, which is derived from Eqs. (5) and (10) in the limits of $k_{\parallel}=0$ and $k_{\perp}\rho_{te} \ll 1$. Thus, it is considered that the formation of the isolated vortices and their mergers found in the slab ETG turbulence reflect the similarities between the gyrokinetic and the HM equations. In the ITG case with the zonal-flow generation [Fig. 5(c)], an anisotropic flow structure dominated by the strong zonal flow ($k_x \approx 0.4, k_y=0$) is observed, where the amplitude of the zonal-flow potential is $|\delta\phi|_{\text{zonal}} \approx 2[\rho_{ti}T_i/L_T e]$. The slab ITG driven zonal flows with the large amplitude and its strong flow shear completely suppress the turbulent transport.

C. Transition of vortex structure and transport reduction

Here, we discuss the results of the slab ETG turbulence simulation in case 2, which is linearly more unstable in comparison with case 1. The entropy balance relation is also satisfied in the present case. However, we find quite different behavior of the electron heat flux and the vortex structures as shown below.

Figure 6 shows the time evolutions of electron heat transport coefficients for case 1 and case 2. As the linear dispersion relation for case 2 shows the larger growth rate and the wider range of unstable modes than those in case 1, one finds earlier saturation and higher transport level at $t \leq 3000$. In case 2, however, a transition of vortex structure, which will be shown in Fig. 8, occurs from a turbulent to a coherent states accompanied with the significant reduction of transport level at $t \sim 3500$. In contrast, case 1 keeps the

TABLE II. Time averaged heat transport coefficients in case 2.

	$\overline{\chi_e}[\rho_{te}^2 v_{te}/L_T]$	Averaging time
Turbulent state	3.37×10^{-1}	$1000 \leq t \leq 3000$
Coherent state	1.77×10^{-2}	$6000 \leq t \leq 8000$

steady transport level of $\overline{\chi_e} = 4.65 \times 10^{-2} [\rho_{te}^2 v_{te}/L_T]$ for $t \geq 6000$. The time averaged heat transport coefficients for case 2 in the turbulent and coherent states are summarized in Table II. Surprisingly, the transport level in the coherent state of case 2 is about 2.6 times less than the steady transport level in case 1 with a relatively moderate growth rates of the linear ETG modes. The reversal of transport level between case 1 and case 2 is expected from neither quasilinear theory nor mixing-length estimates. Since zonal flows play a major role in realizing the steady χ_e as shown in Fig. 3, we consider that the onset of the transition of the transport level also depends on the zonal-flow amplitude.

Comparisons of the time evolutions of the potential energy for case 1 and case 2 are shown in Figs. 7(a) and 7(b), where the total potential energy W in Eq. (13) is divided into zonal flow and turbulence components defined by $W_{zf} \equiv \sum_{k_x} W_{k_x, k_y=0}$ and $W_{trb} \equiv \sum_{k_x} \sum_{k_y \neq 0} W_{k_x, k_y}$, respectively. In Fig. 7(a), we see that the turbulence energy W_{trb} in the both cases gradually increase after the initial saturation of the ETG instability; then they reach to steady states at $t \geq 5200$. The time averaged values are $\overline{W_{trb}} = 8.99 [(\rho_{te}/L_T)^2 (T_e/e)^2]$ for case 1 and $\overline{W_{trb}} = 12.6 [(\rho_{te}/L_T)^2 (T_e/e)^2]$ for case 2, respectively, where the time averages are taken for $5200 \leq t \leq 8000$. Evolutions of the zonal-flow energy W_{zf} are quite different between case 1 and case 2 as shown in Fig. 7(b). In

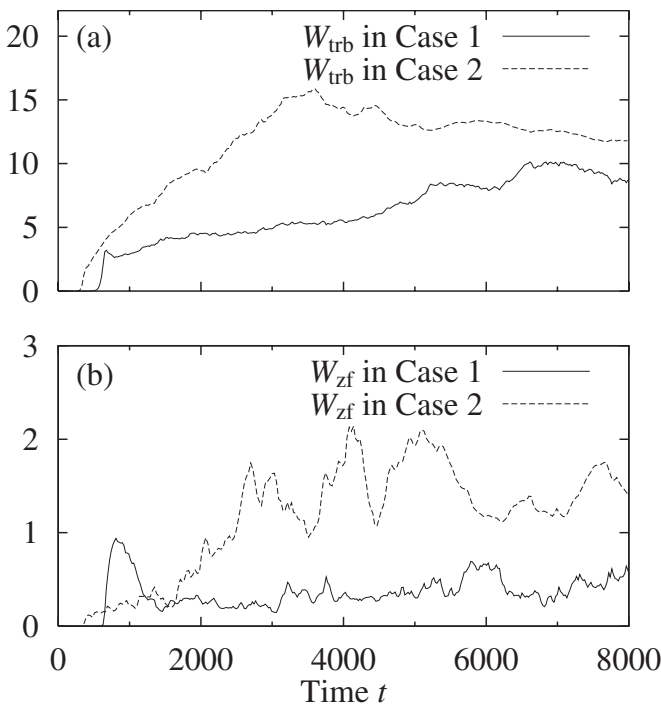


FIG. 7. Time evolutions of (a) turbulence energy W_{trb} and (b) zonal-flow energy W_{zf} in case 1 and case 2, where the units $(\rho_{te}/L_T)^2 (T_e/e)^2$ are used.

case 1, the nonlinearly generated zonal flows increase exponentially at $t \leq 810$. After that, the zonal-flow energy, however, decays quickly and keeps a steady level of $\overline{W_{zf}} = 0.428 [(\rho_{te}/L_T)^2 (T_e/e)^2]$, where the time averages are taken for $6000 \leq t \leq 8000$. In contrast to case 1, the zonal-flow energy for case 2 continue to increase gradually until $t \sim 2700$. Finally, it sustains about 3.2 times higher level of $\overline{W_{zf}} = 1.36 [(\rho_{te}/L_T)^2 (T_e/e)^2]$ than in case 1. The higher level of the zonal-flow energy found in case 2 is associated with the stronger linear ETG instability, causing the higher level of turbulence energy that is a source of zonal flows. Furthermore, the smaller value of the parameter $\Theta (=k_{\parallel}/k_y)$, which denotes the normalized parallel wavenumber, may also be related to the stronger zonal-flow generation. The different behaviors of the zonal-flow energy between case 1 and case 2 lead to the different evolutions of χ_e with the steady level or the transport reduction, as shown in Fig. 6.

Figures 8(a)–8(d) show color contours of potential and temperature fluctuations found in case 2 in the turbulent state at $t=2400$ and the coherent state at $t=7800$, respectively, where the temperature fluctuations are defined by $\delta T_k = \int dv_{\parallel} (v_{\parallel}^2 - 1) \delta f_k$. In the turbulent state, the spatial structures of the both fluctuations are nearly isotropic on the x - y plane [Figs. 8(a) and 8(c)]. Moreover, the temperature fluctuations contain finer spatial-scale components than those in the potential fluctuations. The generation of the fine-scale fluctuations reflects development of the fine-scale structures of the distribution function in the phase-space. On the other hand, in the coherent state, vortex streets along the strong zonal flow are observed in the potential and temperature fluctuations [Figs. 8(b) and 8(d)], which are almost in-phase. A low wavenumber mode with $k_x=0.05$ and $k_y=0.15$ and the zonal-flow component with $k_x=0.15$ and $k_y=0$ mainly contribute to the formation of coherent vortex streets, where they have the comparable amplitude of $|\delta \phi_{k_x=0.05, k_y=0.15}| = 0.664 [(\rho_{te}/L_T) (T_e/e)]$ and $|\delta \phi_{k_x=0.15, k_y=0}| = 0.598 [(\rho_{te}/L_T) \times (T_e/e)]$. The coherent vortex streets slowly propagate in the ion diamagnetic direction (the negative y -direction), which is opposite to the propagation direction of the linear ETG modes. Moreover, the fine-scale structures of temperature fluctuations disappear in the coherent state, while the amplitude is as large as that in the turbulent state.

In order to find a relation between the transition of vortex structure and transport level, the power spectra of $\delta \phi_k$, δT_k , and χ_{ek} are shown in Figs. 9(a)–9(c), respectively, where the quantities are summed over k_x components and the time averages are taken for $1000 \leq t \leq 3000$ in the turbulent state and for $6000 \leq t \leq 8000$ in the coherent state. The low wavenumber components of $|\delta \phi_k|$ for $k_y \leq 0.2$ in the coherent state are slightly larger than those in the turbulent state, while the higher wavenumber components for $k_y \geq 0.25$ significantly decrease by a factor of 3–10. On the other hand, the amplitude of $|\delta T_{k_y}|$ for all k_y in the coherent state is less than that in the turbulent state, where the reduction in high wavenumber components for $k_y \geq 1.0$ is significant. These features are consistent with the coherent structures shown in Figs. 8(b) and 8(d), where the fine-scale fluctuations in $\delta \phi$ and δT are smoothed out. It is noteworthy that the low wave-

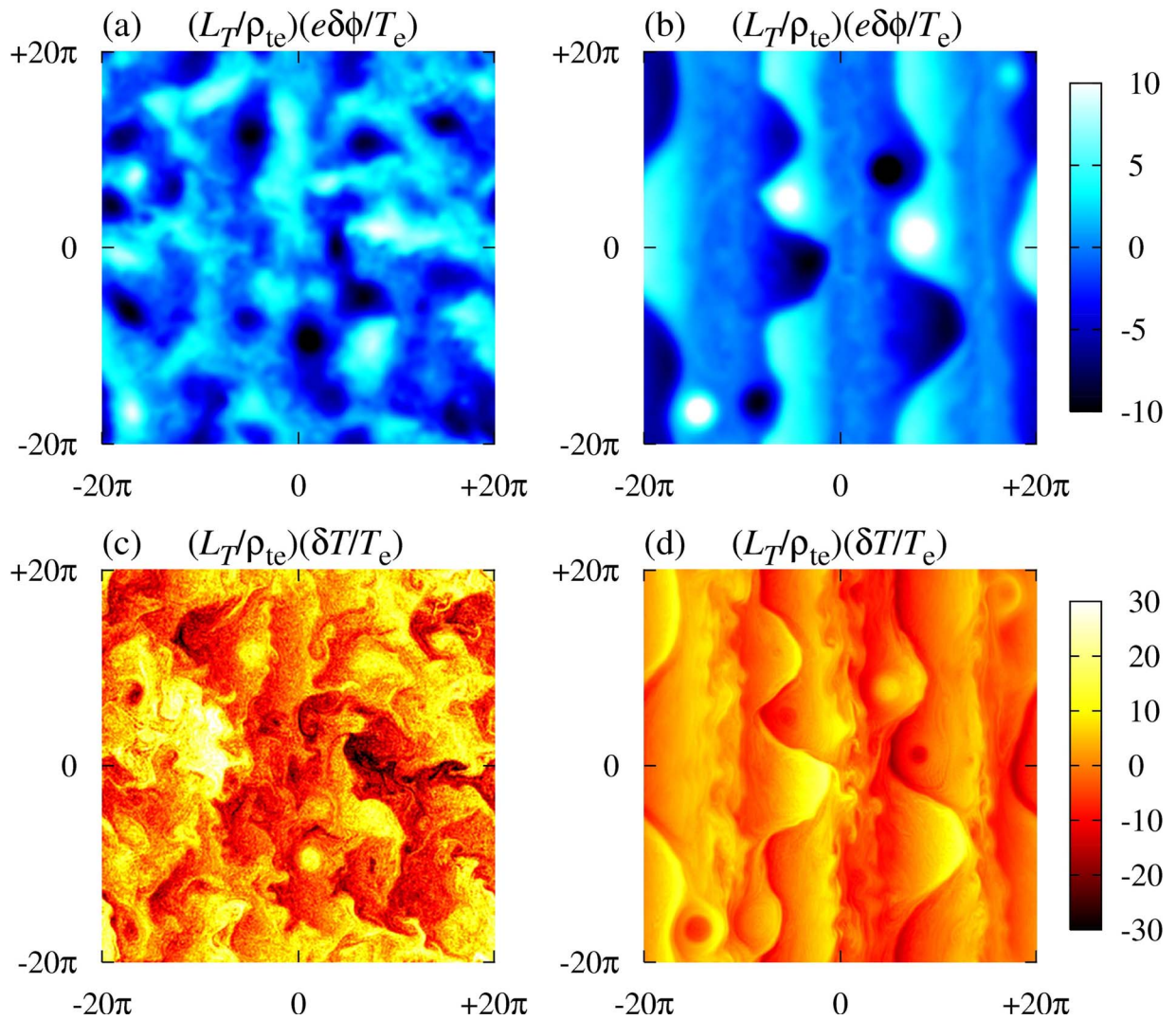


FIG. 8. (Color online) Contours of normalized potential fluctuations at (a) $t=2400$ (turbulent state) and (b) $t=7800$ (coherent state) and normalized temperature fluctuations at (c) $t=2400$ (turbulent state) and (d) $t=7800$ (coherent state) for case 2.

number components of $|\chi_{ek}|$ around $k_y=0.1$, which make dominant contributions to the total heat transport, decrease by a factor of 15.9 in the coherent state, while the changes in amplitudes of low wavenumber components of $|\delta\phi_{k_y}|$ and $|\delta T_{k_y}|$ are within a factor of 3. The above results for case 2 suggest that the transport reduction in the coherent state is mainly associated with a decrease in phase difference between $\delta\phi_k$ and δT_k rather than the reduction in fluctuation amplitudes. Indeed, the transport coefficient χ_{ek} can be expressed as [see Eq. (14)]

$$\begin{aligned} \chi_{ek} &= -e^{-b_k/2} k_y |\delta\phi_k|^2 \int dv_{\parallel} (v_{\parallel}^2 - 1) \text{Im} \left[\frac{\delta f_k}{\delta\phi_k} \right] \\ &= -e^{-b_k/2} k_y |\delta\phi_k|^2 \text{Im} \left[\frac{\delta T_k}{\delta\phi_k} \right], \end{aligned} \quad (16)$$

where normalized quantities are used here. The above equation shows that the transport coefficient is proportional to the squared amplitude $|\delta\phi_k|^2$ and the imaginary part of the distribution function (or temperature fluctuation) divided by the potential fluctuation $\text{Im}[\delta f_k/\delta\phi_k]$ {or $\text{Im}[\delta T_k/\delta\phi_k]$ }. In gen-

eral, the phase difference $\Delta\theta_k$ between two Fourier modes X_k and Y_k is given by $\Delta\theta_k = \sin^{-1}(\text{Im}[Y_k/X_k])$. Thus, velocity moments of the quantity $\text{Im}[\delta f_k/\delta\phi_k]$ are related to the phase difference between potential fluctuations and other fluid variables. The reduction in the phase difference between potential and pressure fluctuations in the coherent vortex structures dominated by zonal flows has also been observed in gyrofluid simulations of sheared-slab ETG turbulence with small magnetic shear parameter $\hat{s}=0.1$.^{17,18}

In the present gyrokinetic simulation study, the transition of vortex structure from a turbulent to a coherent state, which is accompanied with the reduction in the phase difference between $\delta\phi$ and δT , is related to velocity-space structures of the perturbed distribution function or, especially, to its imaginary part. Figure 10 shows velocity-space profiles of the quantity $-\text{Im}[\delta f_k/\delta\phi_k]$ in Eq. (16). Here, the solid and dashed lines correspond to the results in turbulent and coherent states, respectively, where the modes giving the dominant contribution to the heat transport ($k_x=0$, $k_y=0.1$) are plotted. The linear eigenfunction is also shown by the dotted line in the figure, where a scale factor of 1/2 is multiplied. One

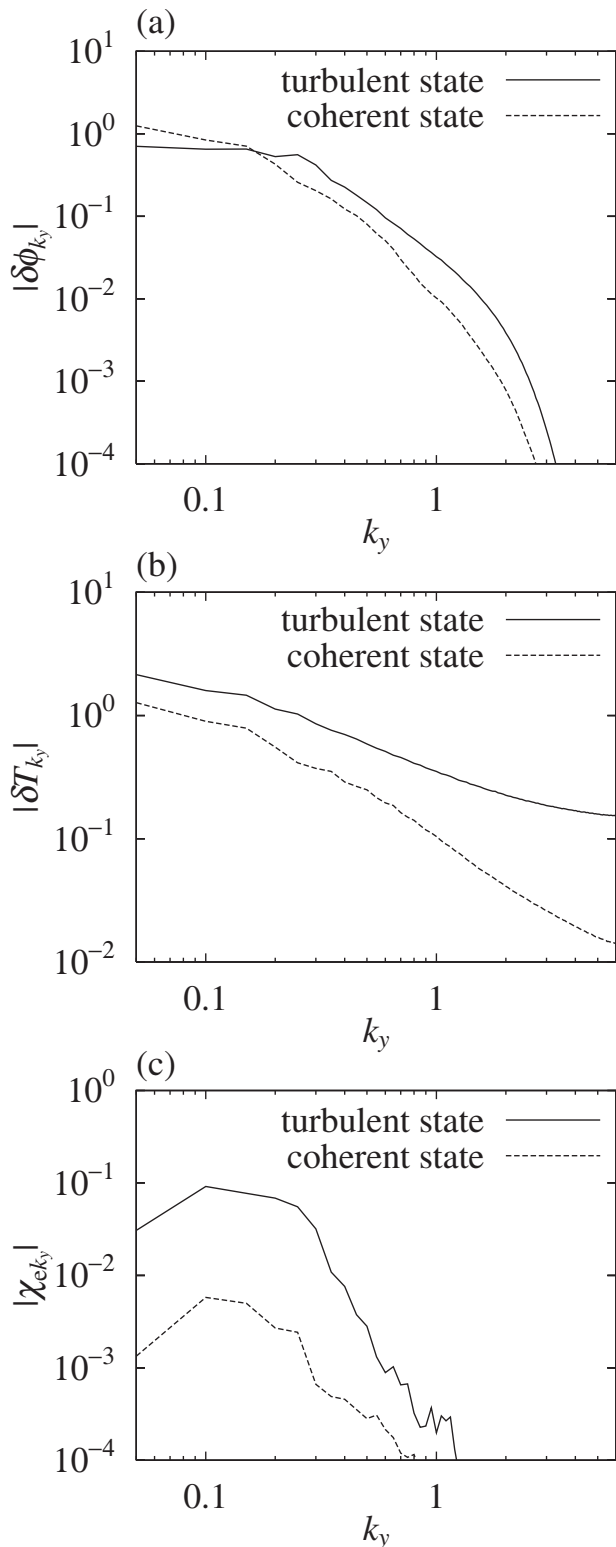


FIG. 9. Power spectra of (a) $|\delta\phi_k|$, (b) $|\delta T_k|$ and (c) $|\chi_{ek}|$ in the turbulent ($1000 \leq t \leq 3000$) and coherent ($6000 \leq t \leq 8000$) states, where the quantities are summed over k_x components and taken time averages.

can see that the profile in turbulent state is qualitatively similar to the linear eigenfunction, which can drive large heat transport. In contrast, the significant decrease in $-\text{Im}[\delta f_k / \delta\phi_k]$ is found in the coherent state, which is related to the transport reduction. The decrease in $-\text{Im}[\delta f_k / \delta\phi_k]$

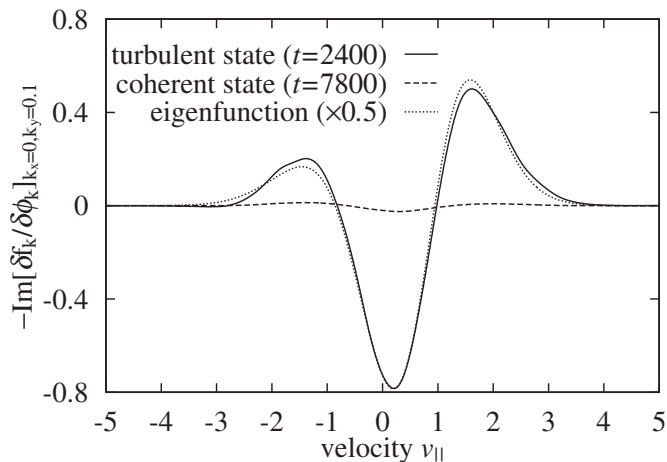


FIG. 10. Velocity-space profiles of the quantity $-\text{Im}[\delta f_k / \delta\phi_k]$ for the mode giving the dominant contribution to the heat transport ($k_x=0$, $k_y=0.1$).

corresponds to the phase matching of $\delta\phi$ and δT , and it is consistent with the spatial structures shown in Figs. 8(b) and 8(d). Furthermore, the smaller value of $-\text{Im}[\delta f_k / \delta\phi_k]$ in the coherent state suggests that the reduction in phase difference to potential fluctuations $\delta\phi_k$ is found not only for temperature fluctuations δT_k but also for any n th velocity moments of the perturbed distribution function $\delta M_k^{(n)} \equiv \int dv_{||} v_{||}^n \delta f_k$. This fact is utilized for a derivation of a model equation describing the coherent vortex streets.

The results of nonlinear simulations suggest that the onset of the transition to the coherent state and the formation of vortex streets, which are accompanied with the phase matching phenomena, is closely related to the behavior of zonal flows. It depends on the parameters $\eta_e \equiv L_n / L_T$ and $\Theta \equiv k_{||} / k_y$, which determine the linear ETG instability in the present model with the fixed ν_e and $\tau \equiv T_i / T_e$. In particular, the parameter Θ , which is relevant to the parallel electron flows, is considered to be influential on the growth of zonal flows through nonlinear mode couplings with $k_{||} \neq 0$ modes. It has also been pointed out that the parallel electron flows are essential to the stabilization of the Kelvin–Helmholtz modes for zonal flows.¹⁵ A comprehensive parameter-scan remains for a future work to clarify which parameters are favorable for the strong zonal-flow generation and the formation of the coherent vortex structures. These analyses are expected to contribute to finding a critical condition for the transition of vortex structures from turbulent to coherent states with transport reduction and may provide ones a useful insight in relation to the chaos-or turbulence-control. In fact, by means of the Hasegawa–Wakatani model, Klinger *et al.*²⁹ pointed out that an externally applied perturbation of the parallel flow leads to the transition from the drift wave turbulence to a coherent state.

The simple shear-less slab configuration with constant Θ used in the present study is associated with a local model for the neighborhood of the minimum- q surface (q denotes the safety factor), which has a weak magnetic shear $\hat{s} \ll 1$, in the toroidal system with a reversed magnetic shear profile.^{5,6} In the case with a weak magnetic shear, each position of the rational surface becomes more distant, and the toroidal-mode

couplings weaken so that the slab ETG modes can also be destabilized. Actually, the global gyrokinetic PIC simulations of the slab ETG turbulence for the reversed magnetic shear profile have found out the strong zonal-flow generation and the significant reduction in the electron heat transport around the minimum- q surface where the \hat{s} vanishes.¹⁵ Extension of the present work to toroidal configurations will be pursued to explore the possibility of the coherent vortex structure formation and the transport reduction under realistic conditions.

IV. ANALYSIS OF COHERENT VORTEX STREETS

A. HM type model for coherent vortex streets

Here, we derive a model equation by which the coherent vortex streets shown in the previous section can be described. It can also be utilized for the detailed comparison with nonlinear simulation results.

Main features of the coherent vortex streets with significantly low transport level found in the previous section are summarized as follows. First, the spatial profile of $\delta\phi$ mainly consists of large-scale vortices and zonal flows with comparable amplitudes [see Fig. 8(b)]. Second, the propagating direction of these vortices is opposite to that of the linear ETG modes. Third, the phase matching occurs between the potential fluctuation $\delta\phi_{\mathbf{k}}$ and the fluctuations $\delta M_{\mathbf{k}}^{(n)}$ defined by the n th velocity moments of the perturbed distribution function. These features allow us to derive a fluid equation for the coherent vortex streets. By taking the v_{\parallel} -space integral of gyrokinetic equation in Eq. (6) and by use of the quasineutrality condition in Eq. (11), one can obtain the following equation:

$$\begin{aligned} \frac{\partial}{\partial t} \Lambda_{\mathbf{k}} \delta\psi_{\mathbf{k}} - ik_y \left(1 - \frac{b_{\mathbf{k}}}{2} \eta_e \right) \delta\psi_{\mathbf{k}} \\ - \sum_{\mathbf{k}=\mathbf{k}'+\mathbf{k}''} \mathbf{b} \cdot (\mathbf{k}' \times \mathbf{k}'') \delta\psi_{\mathbf{k}'} \Lambda_{\mathbf{k}''} \delta\psi_{\mathbf{k}''} = 0, \end{aligned} \quad (17)$$

which is formally similar to the HM equation written in the wavenumber space. Here, the moment of parallel advection term $\int dv_{\parallel} ik_{\parallel} v_{\parallel} \delta f_{\mathbf{k}} (= ik_{\parallel} u_{\parallel})$, which causes the linear ETG instability through a coupling with higher order moments, is neglected for simplicity because it is relatively smaller than the other terms in the coherent state. The validity for neglecting the parallel advection term will be discussed in Sec. IV B. The FLR-factor is denoted by $\Lambda_{\mathbf{k}} \equiv e^{b_{\mathbf{k}}} \{1 + \tau - \Gamma_0(b_{\mathbf{k}})\}$. Normalizations are the same as shown in Sec. II, except that the macroscopic gradient scale length is changed from L_T into L_n for comparison with the original HM equation. The original HM model is derived from fluid equations for cold ions ($T_i \rightarrow 0$) with the adiabatic electron response; then the model describes the density gradient driven drift waves. In contrast to the original HM model, Eq. (17) is derived from the gyrokinetic equation for electrons with the adiabatic ion response and includes the ETG η_e described by $ik_y (b_{\mathbf{k}} \eta_e / 2) \delta\psi_{\mathbf{k}}$, which does not appear in the cold-electron limit ($T_e \rightarrow 0$). Hereafter, an abbreviation for our model in Eq. (17) is denoted by ‘‘HM- η_e model’’ for convenience. Similarly to the original HM model, the HM- η_e model also has no source driving linear instabilities.

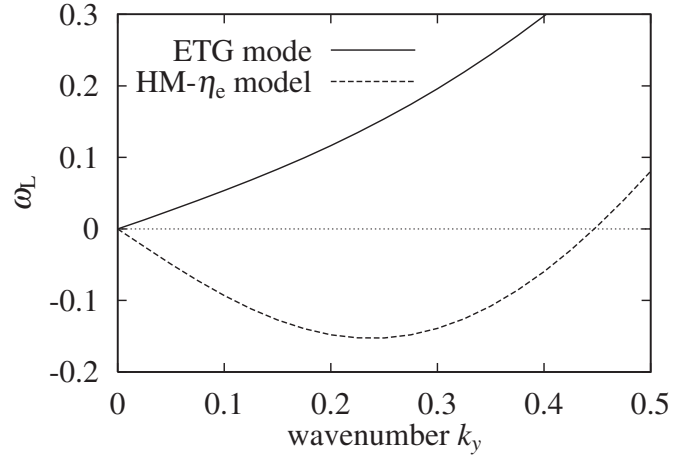


FIG. 11. Comparison of the real frequencies $\omega_L(k_x=0, k_y)$ between the linear ETG modes and HM- η_e model, where ω_L is normalized by v_{te}/L_n .

Figure 11 shows the comparison of real frequencies for $k_x=0$ between the linear ETG mode described by the gyrokinetic model and linear drift waves described by the HM- η_e model. The real frequency for the HM- η_e model is given by

$$\omega_L = \frac{-e^{-b_{\mathbf{k}}} k_y}{1 + \tau - \Gamma_0(b_{\mathbf{k}})} \left(1 - \frac{\eta_e}{2} b_{\mathbf{k}} \right). \quad (18)$$

We see that the real frequencies in HM- η_e model have negative values for the low wavenumber modes of $k_y \leq \sqrt{2/\eta_e} \approx 0.447$, while the ETG modes have positive real frequencies for all modes. The negative frequency means that the direction of the mode propagation is opposite to that of the linear ETG modes. Indeed, as described in the previous section, the coherent vortex streets propagate in the negative y -direction.

In the long wavelength limit of $k_{\perp} \rho_{te} \ll 1$, Eq. (17) is represented in the real space as follows:

$$\begin{aligned} \frac{\partial}{\partial t} \{ \tau - (1 + \tau) \nabla_{\perp}^2 \} \delta\psi - \frac{\partial}{\partial y} \left(1 + \frac{\eta_e}{2} \nabla_{\perp}^2 \right) \delta\psi \\ - [\delta\psi, (1 + \tau) \nabla_{\perp}^2 \delta\psi] = 0, \end{aligned} \quad (19)$$

where the square brackets denote the Poisson brackets $[A, B] = (\partial_x A)(\partial_y B) - (\partial_x B)(\partial_y A)$. An isomorphic form to the original HM equation, which has an opposite sign of the drift frequency, is derived by taking a cold-electron limit $T_e \rightarrow 0$ and $\eta_e \rightarrow 0$. In analogy with the HM model having a traveling wave solution,³⁰ e.g., isolated dipole vortices, one can derive a condition for the traveling wave solution of the HM- η_e equation in the long wavelength limit. Suppose the potential fluctuation in $\delta\psi = \delta\psi(x, y - ut)$ in Eq. (19) with constant traveling velocity parameter u ; then the time derivative is replaced with the y -derivative, $\partial_t \delta\psi = -u \partial_y \delta\psi = [-ux, \delta\psi]$. After some simple algebra, one finds the following equation:

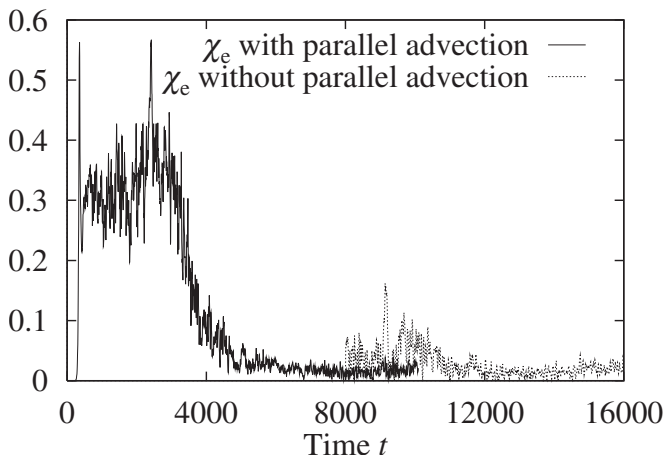


FIG. 12. Comparison of the time evolutions of χ_e with and without the parallel advection term.

$$[S_1, S_2] \equiv \left[\nabla_{\perp}^2 \delta\psi - \left(\frac{1 + \tau u}{1 + \tau} \right) x, \delta\psi - \left\{ u - \frac{\eta_e}{2(1 + \tau)} \right\} x \right] = 0. \tag{20}$$

This condition shows that $\delta\psi$ is a traveling wave solution of the HM- η_e equation if there is a functional relation between S_1 and S_2 , i.e., $S_1 = F(S_2)$ with an arbitrary function F . The analysis of the functional dependence on S_1 and S_2 is similar to that demonstrated in two-dimensional rotating fluid turbulence by Jung and Morrison *et al.*³¹ They introduced a method of averaging the stream function that allows them to find the linear functional relation of the generalized vorticity and the stream function clearly. In the present study, we investigate the functional relation between S_1 and S_2 as a measure for characterizing the coherent vortex streets to be a traveling wave solution of the HM- η_e equation.

B. Comparison between HM- η_e model and simulation results

In this section, the coherent vortex streets found in the gyrokinetic simulation for case 2 is compared with the traveling wave solution of HM- η_e equation. In order to confirm the validity for neglecting the parallel advection term in the derivation of HM- η_e model in Eq. (17) [or Eq. (19)] for the coherent vortex streets, we compare gyrokinetic simulation results for cases with and without the parallel advection term $ikv_{\parallel} \delta f_k$. Figure 12 shows the time evolution of χ_e , where the solid line is the same as that shown in Fig. 6 for case 2. The dotted line corresponds to the result where the parallel advection term is artificially eliminated in the coherent state at $t=8000$ and later. Although the initial increase in χ_e arisen from the discontinuity of the parallel advection term are observed for $8000 \leq t \leq 10\,000$, the long-time behavior of χ_e for $t \geq 10\,000$ shows the quite low transport level, which is the same level as that in the coherent state at around $t=8000$ shown by the solid line.

Snapshots of vortex structures for the cases with and without the parallel advection term are compared in Figs. 13(a) and 13(b), respectively, where the gyroaveraged poten-

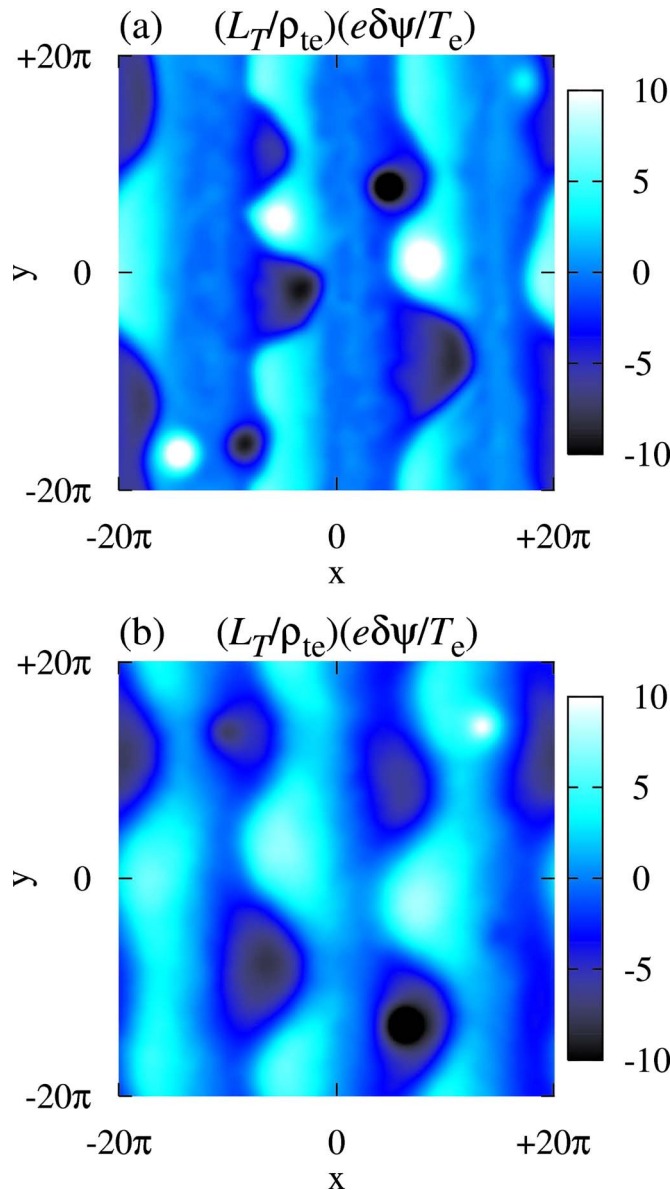


FIG. 13. (Color online) Contours of the gyroaveraged potential with the parallel advection term at (a) $t=7800$ and without one at (b) $t=16\,000$.

tials $\delta\psi$ are plotted by color contours. In Fig. 13(b), one finds that the vortex streets found in the coherent state at $t=7800$ [Fig. 13(a)] sustain its spatial structure for a long time after eliminating the parallel advection term. Also, the vortices propagate in the negative y -direction, which is consistent with the negative real frequency for low wavenumber modes of the HM- η_e model. These results justify neglecting the parallel advection term in the derivation of HM- η_e model for the coherent vortex streets. In addition, the propagation of the vortices keeping the spatial structure suggests that the coherent vortex streets are described by a traveling wave solution of Eq. (19).

Direct evaluations of the functional relation of S_1 and S_2 in Eq. (20) are shown in Figs. 14(a) and 14(b) for the non-linear simulation results in case 2, where the traveling velocity parameter $u \approx -\pi/4$ is estimated from the simulation results. Here, we used simulation data taken from $+3\pi \leq x$

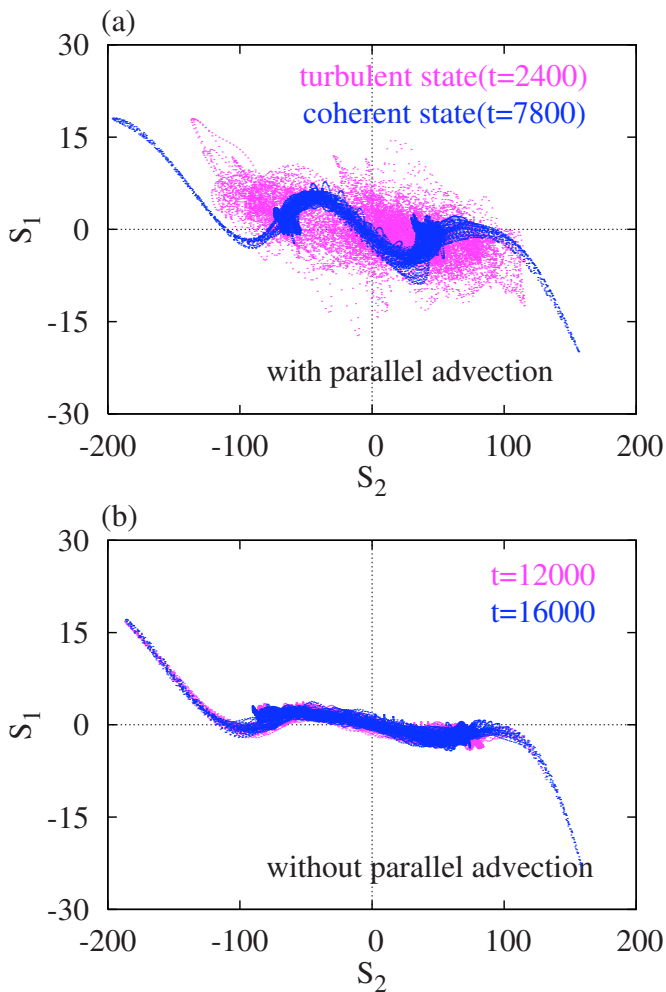


FIG. 14. (Color online) Puncture plots for S_1 vs S_2 given in Eq. (20), where the plots correspond to the cases (a) with and (b) without the parallel advection term, respectively.

$\leq +15\pi$ [see Fig. 13(a)] for the single vortex street on the right side of simulation domain because the vortices on the left side propagate with slightly different speed. The puncture plots of S_1 versus S_2 in the turbulent ($t=2400$) and coherent ($t=7800$) states are shown in Fig. 14(a). A nonlinear functional relation between S_1 and S_2 is clearly found in the coherent state, while the dot pattern broadens and looks disturbed in the turbulent state. The same plots are made for the simulation without the parallel advection term, which corresponds to a simulation of HM- η_e model [Fig. 14(b)]. One can see that the nonlinear functional relation, which is similar to that in the coherent state shown in Fig. 14(a), is apparently sustained for a long time. The puncture plot for the coherent state in Fig. 14(a) clearly shows the qualitative agreement with that in Fig. 14(b) even with a stronger curvature in the functional relation between S_1 and S_2 . Therefore, it is concluded that the coherent vortex streets found in the slab ETG turbulence for case 2, which leads to the transport reduction, are described by a traveling wave solution of the HM- η_e equation.

V. CONCLUDING REMARKS

We have investigated the vortex structure and related transport reduction in the slab ETG turbulence by means of the gyrokinetic Vlasov simulation. The nonlinear simulations with high phase-space resolution enable us to examine the entropy balance relation, detailed structures of distribution function in the velocity-space, and coherent vortex structures of fluid variables, e.g., potential and temperature fluctuations, which have rarely been discussed in earlier studies on ETG turbulence.

The evaluation of entropy balance relation in the slab ETG turbulence with a moderate linear growth rate (case 1) shows that the turbulence reaches to the statistically steady state accompanied with weak zonal-flow generations. Through the comparison of the slab ETG (with and without zonal flows) and the slab ITG turbulence simulations, it is found that the zonal flows driven by the slab ETG turbulence play a crucial role in suppressing the $(k_x=0, k_y=k_{\min})$ -mode and in realizing the steady χ_e . The formation of isolated vortices and their mergers with complicated motion are observed in the slab ETG turbulence, while the slab ITG turbulence is dominated by strong zonal flows, which completely suppress the turbulent transport.

In the slab ETG turbulence with larger growth rates (case 2), we observed a transition of the vortex structure from a turbulent state with finer-scale fluctuations to a coherent state dominated by coherent vortex streets, which are composed of large-scale vortices and strong zonal flows. At the same time, the turbulent transport reduces to a quite low level, which is less than the time averaged χ_e in case 1. The spectral analysis of $|\delta\phi_k|$, $|\delta T_k|$, and $|\chi_{ek}|$ in the wavenumber space shows that the transport reduction in the coherent state is mainly associated with a decrease in phase difference between $\delta\phi_k$ and δT_k , not with the reduction in the amplitudes. The transport reduction through the phase matching is confirmed more clearly by the velocity-space plots of $-\text{Im}[\delta f_k / \delta\phi_k]$. The amplitude of $-\text{Im}[\delta f_k / \delta\phi_k]$ is quite small in the coherent state, while its profile in the turbulent state is qualitatively similar to the linear eigenfunction, which drives large heat transport. Furthermore, the smallness of $-\text{Im}[\delta f_k / \delta\phi_k]$ in the coherent state shows that the phase matching with $\delta\phi_k$ occurs not only for δT_k but also for any n th velocity moments of the perturbed distribution function, i.e., $\delta M_k^{(n)} \equiv \int dv_{\parallel} v_{\parallel}^n \delta f_k$.

In order to describe the coherent vortex streets, we have derived a fluid model from the gyrokinetic equation, where the velocity moment of the parallel advection term $\int dv_{\parallel} i k_{\parallel} v_{\parallel} \delta f_k$ is ignored. The validity of neglecting the parallel advection term in the derivation has been confirmed by comparisons of the nonlinear simulations. In addition to a formal similarity to the original HM equation, the HM- η_e model derived in Eq. (19) involves the ETG term. By evaluating the functional relation of S_1 and S_2 [see Eq. (20)] from the nonlinear simulation results, it is concluded that the coherent vortex streets found in the slab ETG turbulence, which are related to the transport reduction, are explained by a traveling wave solution of HM- η_e equation.

It is considered that the formation of coherent structures

such as vortex streets is strongly related to the behavior of zonal flows, which depend on parameters η_e and Θ . The parameter Θ related to the parallel electron dynamics is also expected to be important for the zonal-flow generation and its stability. In order to clarify which parameters are favorable for the formation of the coherent vortex structures and the transport reduction, one needs to perform a comprehensive parameter scan, which remains for future works. Although the simple shearless slab configuration has been used in the present study, it is considered to be associated with a local model for a weak magnetic shear region in the toroidal system. Extension of the present work to the toroidal configuration is currently in progress and will be reported elsewhere.

ACKNOWLEDGMENTS

Numerical computations are performed on the NIFS Plasma Simulator and supercomputing resources at Cyber-science Center, Tohoku University.

This work was supported in part by the Grant-in-Aid for Japan Society for the Promotion of Science (Grant No. 20-4017), in part by the Japanese Ministry of Education, Culture, Sports, Science, and Technology, Grant No. 21560861, and in part by the NIFS Collaborative Research Programs, Grant Nos. NIFS08KNXN145, NIFS08KDAD008, NIFS08KTAL006, and NIFS09KTAL022.

¹W. Horton, *Rev. Mod. Phys.* **71**, 735 (1999).

²A. M. Dimits, G. Bateman, M. A. Beer, B. I. Cohen, W. Dorland, G. W. Hammett, C. Kim, J. E. Kinsey, M. Kotschenreuther, A. H. Kritiz, L. L. Lao, J. Mandrekas, W. M. Nevins, S. E. Parker, A. J. Redd, D. E. Shumaker, R. Sydora, and J. Weiland, *Phys. Plasmas* **7**, 969 (2000).

³P. H. Diamond, S.-I. Itoh, K. Itoh, and T. S. Hahm, *Plasma Phys. Controlled Fusion* **47**, R35 (2005).

⁴A. Fujisawa, K. Itoh, H. Iguchi, K. Matsuoka, S. Okamura, A. Shimizu, T. Minami, Y. Yoshimura, K. Nagaoka, C. Takahashi, M. Kojima, H. Nakano, S. Oshima, S. Nishimura, M. Isobe, C. Suzuki, T. Akiyama, K. Ida, K. Toi, S.-I. Itoh, and P. H. Diamond, *Phys. Rev. Lett.* **93**, 165002 (2004).

⁵B. W. Stallard, C. M. Greenfield, G. M. Staebler, C. L. Rettig, M. S. Chu,

M. E. Austin, D. R. Baker, L. R. Baylor, K. H. Burrell, J. C. DeBoo, J. S. deGrassie, E. J. Doyle, J. Lohr, G. R. McKee, R. L. Miller, W. A. Peebles, C. C. Petty, R. I. Pinsker, B. W. Rice, T. L. Rhodes, R. E. Waltz, and L. Zeng, and DIII-D Team, *Phys. Plasmas* **6**, 1978 (1999).

⁶H. Shirai, M. Kikuchi, T. Takizuka, T. Fujita, Y. Koide, G. Rewoldt, D. Mikkelsen, R. Budny, W. M. Tang, Y. Kishimoto, Y. Kamada, T. Oikawa, O. Naito, T. Fukuda, N. Isei, Y. Kawano, M. Azumi, and JT-60 Team, *Nucl. Fusion* **39**, 1713 (1999).

⁷F. Jenko, W. Dorland, M. Kotschenreuther, and B. N. Rogers, *Phys. Plasmas* **7**, 1904 (2000).

⁸W. Dorland and G. W. Hammett, *Phys. Fluids B* **5**, 812 (1993).

⁹Y. Idomura, S. Tokuda, and Y. Kishimoto, *Nucl. Fusion* **45**, 1571 (2005).

¹⁰J. Candy, R. E. Waltz, M. R. Fahey, and C. Holland, *Plasma Phys. Controlled Fusion* **49**, 1209 (2007).

¹¹W. M. Nevins, S. E. Parker, Y. Chen, J. Candy, A. Dimits, W. Dorland, G. W. Hammett, and F. Jenko, *Phys. Plasmas* **14**, 084501 (2007).

¹²W. M. Nevins, J. Candy, S. Cowley, T. Dannert, A. Dimits, W. Dorland, C. Estrada-Mila, G. W. Hammett, F. Jenko, M. J. Pueschel, and D. E. Shumaker, *Phys. Plasmas* **13**, 122306 (2006).

¹³Z. Lin, I. Holod, L. Chen, P. H. Diamond, T. S. Hahm, and S. Ethier, *Phys. Rev. Lett.* **99**, 265003 (2007).

¹⁴J. Li, Y. Kishimoto, N. Miyato, T. Matsumoto, and J. Q. Dong, *Nucl. Fusion* **45**, 1293 (2005).

¹⁵Y. Idomura, M. Wakatani, and S. Tokuda, *Phys. Plasmas* **7**, 3551 (2000).

¹⁶Y. Idomura, *Phys. Plasmas* **13**, 080701 (2006).

¹⁷T. Matsumoto, J. Li, and Y. Kishimoto, *Nucl. Fusion* **47**, 880 (2007).

¹⁸T. Matsumoto, Y. Kishimoto, N. Miyato, and J. Q. Li, *J. Plasma Phys.* **72**, 1183 (2006).

¹⁹J. Li and Y. Kishimoto, *Phys. Plasmas* **15**, 112504 (2008).

²⁰T.-H. Watanabe and H. Sugama, *Nucl. Fusion* **46**, 24 (2006).

²¹T.-H. Watanabe and H. Sugama, *Phys. Plasmas* **11**, 1476 (2004).

²²T.-H. Watanabe and H. Sugama, *Phys. Plasmas* **9**, 3659 (2002).

²³H. Sugama, T.-H. Watanabe, and W. Horton, *Phys. Plasmas* **10**, 726 (2003).

²⁴D. H. E. Dubin, J. Krommes, C. Oberman, and W. W. Lee, *Phys. Fluids* **26**, 3524 (1983).

²⁵A. J. Brizard and T. S. Hahm, *Rev. Mod. Phys.* **79**, 421 (2007).

²⁶H. Sugama, M. Okamoto, W. Horton, and M. Wakatani, *Phys. Plasmas* **3**, 2379 (1996).

²⁷J. A. Krommes and G. Hu, *Phys. Plasmas* **1**, 3211 (1994).

²⁸A. Hasegawa and K. Mima, *Phys. Fluids* **21**, 87 (1978).

²⁹T. Klinger, C. Schröder, D. Block, F. Greiner, A. Piel, G. Bonhomme, and V. Naulin, *Phys. Plasmas* **8**, 1961 (2001).

³⁰W. Horton and Y.-H. Ichikawa, *Chaos and Structures in Nonlinear Plasmas* (World Scientific, Singapore, 1996).

³¹S. Jung, P. J. Morrison, and H. L. Swinney, *J. Fluid Mech.* **554**, 433 (2006).